FULL PAPER

Single Molecule with Dual Function on Nanogold: Biofunctionalized Construct for In Vivo Photoacoustic Imaging and SERS Biosensing

U. S. Dinish, Zhegang Song, Chris Jun Hui Ho, Ghayathri Balasundaram, Amalina Binte Ebrahim Attia, Xianmao Lu, Ben Zhong Tang, Bin Liu,* and Malini Olivo**

Multimodal imaging provides complimentary information that is advantageous in studying both cellular and molecular mechanisms in vivo, which has tremendous potential in pre-clinical research and clinical translational imaging. It is desirable to design probes for multimodal imaging that can be administered minimally but provides multifaceted information. Herein, we demonstrate the complementary dual functional ability of a nanoconstruct for molecular imaging in both photoacoustic (PA) and surface-enhanced Raman scattering (SERS) biosensing simultaneously in tandem. To realize this, a group of NIR active organic molecules are designed and synthesized that possess both SERS and PA activity. Nanoconstructs realized by anchoring such molecules onto gold nanoparticles are demonstrated for targeting cancer biomarkers in vivo while providing complimentary information about biodistribution and targeting efficiency. In future, such nanoconstructs could play a major role in identifying surgical margins and also for disease monitoring in translational medicine.

1. Introduction

In vivo molecular imaging and sensing provide the means to study cellular and molecular processes that have tremendous potential in biomedical research and clinical applications.[1,2] Among the various small-animal imaging modalities, even though each technique has its merits and demerits, no single technique is capable of achieving the most important requirements such as high sensitivity, high spatial and temporal resolution, low cost, fast response time, high-throughput, and high multiplexing capability.[3] In small-animal imaging, optical techniques such as fluorescence and bioluminescence provide the best spatial resolution, low cost, and ease of operation, but they are limited by the poor penetration depth (typically few mm). Moreover, fluorescence imaging for in vivo studies is limited by several other factors such as (i) small Stokes shift and broad spectral profile that limit the multiplex sensing in a complex medium, (ii) strong autofluorescence from superficial tissue layers, and (iii) rapid photobleaching of fluorophores.[3–6]

In this context, we demonstrate a dual optical modality molecular imaging and sensing technique by combining photoacoustic imaging (PAI) and surface-enhanced Raman scattering (SERS). PAI is a noninvasive sensitive imaging modality that taps on the benefit of optical techniques along with high-frequency ultra sound in such a way that its key features are benefited and superior to each of the individual imaging techniques.[7–11] PAI is realized through the absorption of a pulsed light by a contrast agent present in the tissue, which causes a rapid and transient temperature rise (in the order of mK), leading to a localized thermo-elastic expansion.[12] When a NIR nanosecond pulsed laser beam is scanned through the target to be imaged, the resultant ultrasonic wave profile can be detected using special transducers. These data can be used to reconstruct 2D or 3D optical absorption maps with high spatial resolution (<100 μm) and with a penetration depth up to a few

Dr. U. S. Dinish, Dr. C. J. H. Ho, Dr. G. Balasundaram, Dr. A. B. E. Attia, Prof. M. Olivo
Bio-Optical Imaging Group
Singapore Bioimaging Consortium (SBIC)
Agency for Science, Technology and Research, Singapore
11 Biopolis Way, #01–02, Helios, Singapore 138667
E-mail: malini_olivo@sbic.a-star.edu.sg
Z. Song, Prof. B. Z. Tang
Department of Chemistry, Division of Biomedical Engineering
The Hong Kong University of Science and Technology
Clear Water Bay, Kowloon, Hong Kong
E-mail: tangbenz@ust.hk
DOI: 10.1002/adfm.201404341
Prof. X. Lu, Prof. B. Liu
Department of Chemical and Biomolecular Engineering
4 Engineering Drive 4, National University of Singapore
Singapore 117585
E-mail: cheliub@nus.edu.sg
Prof. B. Liu
Institute of Materials Research and Engineering
Agency for Science, Technology and Research (A*STAR), Singapore
3 Research Link, Singapore 117585
Prof. M. Olivo
School of Physics
National University of Ireland
Galway, Ireland

centimeters. Furthermore, laser excitation at multiple wavelengths (multispectral opto-acoustic tomography (MSOT)) will help in generating multispectral spectroscopic imaging of intrinsic and extrinsic molecular species in one go.[13] In PAI, endogenous contrast agents like hemoglobin, melanin, lipids, or a variety of exogenous molecular imaging agents such as carbon nanotubes, small molecules, and metallic nanoparticles can be employed.[14–19] Endogenous contrast agents offer better tissue access and also help in following transient changes, while exogenous agents significantly improve the sensitivity and allow the targeted detection of biochemical species.[20]

On the other hand, SERS is recently being explored as an effective biosensing optical modality for various pre-clinical applications due to its inherent ability to generate enhanced Raman signal from analytes when they are in close proximity to nanoroughened noble metal surfaces like silver (Ag) or gold (Au).[21–24] SERS provides the most promising advantages like multiparameter molecular analysis and multiplexing potential, which is due to the narrow "fingerprint" Raman spectrum unique to the chemical species. The in vivo SERS is realized by SERS-active nanoparticles (NPs) known as SERS nanotags, which are constructed by attaching strong Raman-active reporter molecules (RMs) onto AuNPs[25–28] and encapsulating them in a polyethylene glycol (PEG)/silica/bovine serum albumin shell.[3,29–33] The encapsulation provides the physical robustness, stable signal, protection from the biochemical environment, and means for bioconjugation. These nanotags can be easily functionalized with various receptor moieties for specific and active in vivo targeting of biomarkers.

The most challenging aspect in combining SERS with PAI for in vivo molecular imaging is the realization of chromophore/nanoconstruct, which is simultaneously active at both modalities, i.e., the RMs used to construct SERS nanotag should be PA-active at the desired excitation wavelength. In one of the such pioneering works, Kircher et al. used conventional commercial Raman active molecules such as trans-1,2-bis (4-pyridyl)-ethylene (BPE) attached to AuNPs. In this nanoconstruct, BPE provides the SERS spectrum while the plasmon absorption peak of AuNPs (≈530 nm) is used to generate PA signal. It is obvious that two separate nanomaterials independently act as "excitation probes" for SERS and PAI.[34] Moreover, since the AuNPs absorb light in the visible region, it has limited tissue penetration depth. To overcome this, in the second study, the same research group used Au nanorods (AuNRs), which have longitudinal surface plasmon resonance (LSPR) in the NIR region to construct the nanoprobe and used the LSPR to tap on the PA signal.[20] However, AuNRs have been proved to have poor photostability upon laser illumination[35] and for in vivo SERS application, AuNPs are generally preferred.[36]

So far, there is no report on a single molecule that could be used for simultaneous read outs in both PAI and SERS detection. In this context, we synthesize a group of NIR-active molecules that can act as both SERS and PAI read-out probe simultaneously. The molecular design takes the following factors into consideration: (1) inherently high Raman cross section of cyanine structure; (2) matching the light absorption of the dye and laser excitation to favor surface enhanced resonance Raman scattering (SERRS)[26]; (3) highly symmetric dye structures to minimize Raman bands for potential spectral multiplexing; (4) strong NIR absorption and low fluorescence quantum yield for deep penetration and strong PA signal; and (5) good solubility in polar solvents for bioconjugation. Specifically, we have developed three dye molecules based on the Cy7 core. Changing the heterocycle rings attached to the central core or directly conjugating aromatic rings to the central core is expected to shift the absorption maxima and the characteristic Raman peaks. As a proof-of-concept, we developed a bimodal imaging nanoconstruct by anchoring the synthesized molecules onto AuNPs followed by encapsulation and bioconjugation to target the cancer biomarkers in vivo using a murine xenograft model. Such nanoconstructs demonstrated molecular specific "fingerprint" SERS sensing in vivo, which is complemented with the imaging capability of PA to understand the localization and biodistribution of the particles. Antibody conjugated nanoconstructs (targeted probe) showed maximum tumor localization by ≈6 h after injection while it was ≈24 h in the case of antibody free nanoconstruct (nontargeted probe). Moreover, targeted probe showed longer retention at tumor compared to nontargeted probe, while both probes showed clearance from the mouse body by ≈72 h.

Combination of the superb sensing capability of SERS with deep tissue penetration (≈up to 4–5 cm) of PA imaging at micrometer resolution can be used to sense and visualize small quantities of biomarker expression at various stages of progression or remission of cancer. In future, the complimentary dual functional imaging and sensing capabilities offered by PA and SERS could help in the identification of the tumor tissues residing under the surface of normal tissues to completely remove the microscopic tumor deposits and also in determination of surgical margins in translational research.

2. Results and Discussion

2.1. Synthesis of Cyanine Molecules and their Optical Characterization

All heptamethine cyanine derivatives were synthesized through condensation reaction between bisaldehyde (**1**) and the corresponding indolenine or benzothiazole salts in toluene/n-butanol mixtures (v/v = 3:7).[37] The reactions proceeded at 120 °C for 12 h to yield green to dark green solids, with considerable yields above 80%. Cy7-Cl and Cy7(S)-Cl were synthesized by **1** and **2** under the condition for the condensation reaction mentioned above. Cy7-OTPE was prepared by nucleophilic substitution of the vinyl chlorine on the cyclohexane bridgehead of Cy-Cl with **3** in a strong basic condition[38] (**Scheme 1**). All compounds have been purified and characterized by standard spectroscopic techniques including NMR and high resolution mass spectroscopy (HRMS). The UV–vis absorption and photoluminescence (PL) spectra of all the Cy7 derivatives in dimethyl sulfoxide (DMSO) are provided in Figure S1 and Figure S2, Supporting Information. The absorption maxima of Cy7-Cl, Cy7(S)-Cl, and Cy7-OTPE are at 786, 808, and 778 nm, and their PL spectra show emission maxima at 820, 835, and 805 nm, respectively. This difference clearly demonstrates that the slight modification in molecular structure has obvious impact on their optical properties.

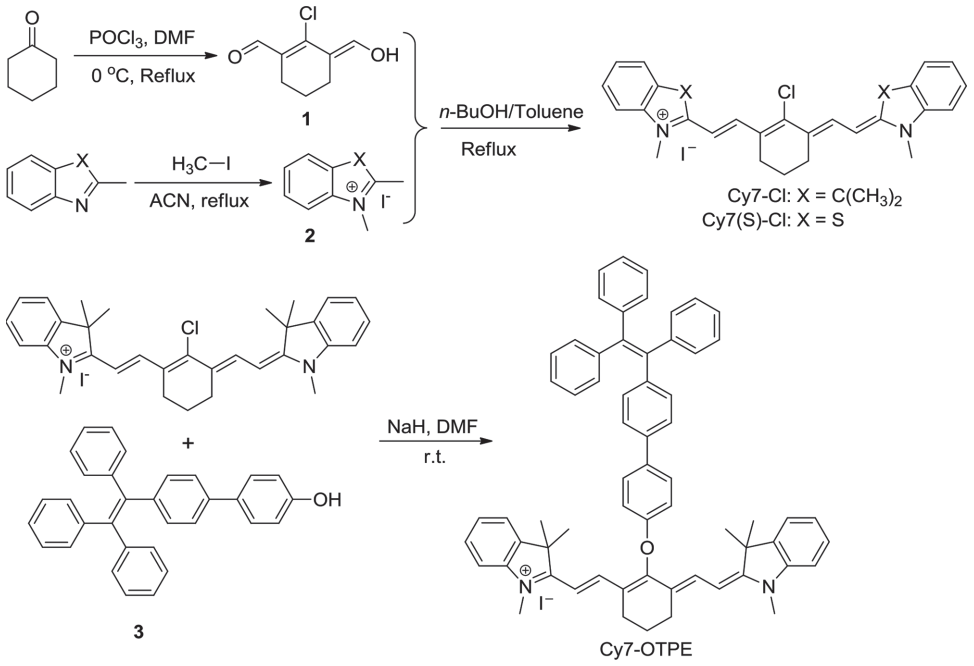

Scheme 1. Synthetic route to Cy7-Cl, Cy7(S)-Cl, and Cy7-OTPE.

2.2. SERS Activity of the Molecules

Initially, we tested the SERS activity of these three molecules (Cy7-Cl, Cy7(S)-Cl, and Cy7-OTPE) after mixing each of them with 60 nm AuNPs and incubating for 15 min. Strong SERS signals were observed even at a low laser power of 50 μW and 10 s integration time as shown in **Figure 1**A. Among these molecules, Cy7-Cl and Cy7-OTPE produced stronger SERS signals while Cy7(S)-Cl produced the weakest signal. Since these molecules possess absorbance in NIR wavelength, 785 nm laser excitation resulted in a strong signal due to SERRS. However, there was fluctuation of the signal intensity. This could be attributed to the nonstable and weaker physisorption of the RMs onto AuNPs, which may lead to desorption from the surface of AuNPs. To avoid this, covalent anchoring of the RMs onto AuNPs is necessary when developing SERS-active NPs for biosensing applications.[26,33]

2.3. PA Activity in Phantom

After demonstrating strong SERS activity of these cyanine molecules, we tested their PA activity in phantom at a concentration of 5×10^{-6} M. As shown in Figure 1B–D, the strong bright spot in the circular well on the left side indicates the PA signal while the right side channel is filled with control solution. It was found that Cy7-Cl (Figure 1B) produced the highest PA signal (6.2×) followed by Cy7-OTPE (Figure 1D, 5.5×), while Cy7(S)-Cl produced the lowest signal (Figure 1C, 3×), which is similar to the trend that was observed in the SERS experiment as well. The strong PA signals on the phantom boundaries was due to the artifacts caused by the mismatches in optical properties between the phantom (made up of polyurethane) and the surrounding water medium, as light is refracted when it crosses the phantom–water interface. This study shows that all three cyanine molecules possess both SERS and PA activity simultaneously. However, due to the physisorption of these molecules on to AuNPs, SERS signals were not stable, which should be addressed when developing the nanoconstruct for in vivo applications. To circumvent this limitation, we chose the

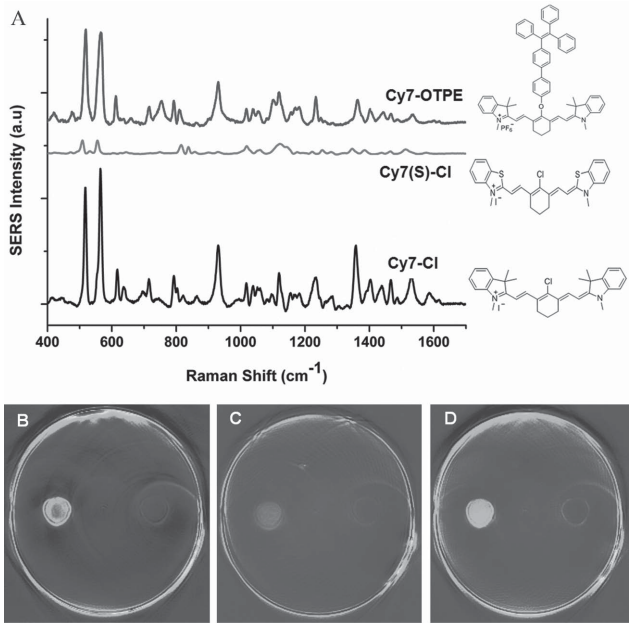

Figure 1. A) SERS spectra of the three cyanine molecules under 785 nm laser excitation. Structures of the molecules are provided. PA signal from B) Cy7-Cl, C) Cy7(S)-Cl, and D) Cy7-OTPE in phantom. In (B–D), the bright spot on the left circle represents the PA signal while the right side circle represents the control.

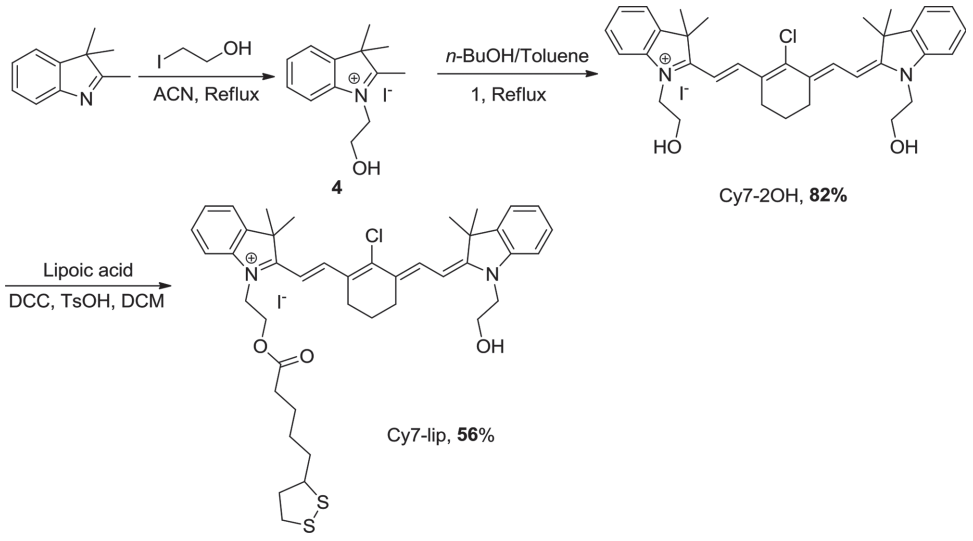

Scheme 2. Synthetic route to Cy7-lip.

best molecule, Cy7-Cl that possesses the highest PA and SERS activity, which is modified to incorporate the lipoic acid (LA) functional group so that it can covalently attach onto AuNPs to generate stable signal.

2.4. Synthesis of Cy7-lip Molecule

Separately, Cy7–2OH was synthesized from **1** and **4**, which was further modified with LA via esterification reaction to furnish Cy7-lip (**Scheme 2**). The product was characterized by standard spectroscopic techniques including NMR and HRMS, which revealed the right structure with high purity (Figures S3–S8, Supporting Information). The final product of Cy7-lip shows similar UV and PL spectra as that of Cy7-Cl indicating that side chain modification does not obviously affect the optical properties of the molecule (Figure S1 and Figure S2, Supporting Information).

2.5. Characterization of Nanoconstruct with Cy7-lip Reporter Molecule

SERS and PA active nanoconstruct was developed by using Cy7-lip as the RM and anchoring it onto AuNPs. In order to realize a stable nanoconstruct, the concentration of the RM anchored on to the AuNPs must be optimized. To understand this, we developed the nanoconstruct at various RM concentrations of 0.1×10^{-6}, 0.5×10^{-6}, 1×10^{-6}, 2×10^{-6}, 3×10^{-6}, 5×10^{-6}, and 10×10^{-6} M. At higher concentrations of the RM, NPs showed aggregation and resulted in lower SERS intensity and also showed non-repeatable absorption spectra. We found that the nanoconstruct with optimized 1×10^{-6} M Cy7-lip concentration resulted in a stable SERS signal. When the concentration of the Cy7-lip was lower than 1×10^{-6} M, SERS and PA signals from the nanoconstruct were weak. Due to the covalent binding of the LA moiety onto AuNPs, the nanoconstruct demonstrated strong SERS signal as shown in **Figure 2**A. Strong SERS intensity of the Cy7-lip molecules is compared to other standard RMs such as malachite green isothiocyanate (MGITC), Cy5, and Rhodamine 6G (Rh6G) under the same experimental conditions (Figure S9, Supporting Information). It demonstrates that Cy7-lip possesses ≈1 order stronger SERS intensity than the next best molecule, which is Cy5. We also monitored the stability of the SERS signal of the Cy7-lip nanoconstruct by measuring the intensity of its most prominent peak (523 cm^{-1}) over a period of 3 weeks. SERS signal intensity was very stable with a reduction of only ≈5% over this period. (Figure S10, Supporting Information).

Any nanoconstruct that possesses absorbance in the NIR region can be used for in vivo PA imaging and our nanoconstruct showed absorbance in the NIR region, as shown in Figure 2B. For comparison, the spectrum of the pure AuNPs is also provided. Subsequently, we measured the PA activity of the nanoconstruct in phantom using the pure AuNPs solution as the control. As shown in Figure 2C, the signal on the left side of the channel confirms the PA activity of the nanoconstruct with ≈5-fold stronger signal as compared to the control solution. Figure 2D shows the transmission electron microscope (TEM) image of the PEG encapsulated nanoconstruct that demonstrates mono-dispersity. The PEG encapsulation will help in minimizing the aggregation along with providing a stable encapsulation layer for the RMs. It was also confirmed that after the encapsulation, the morphology of the particles remained intact with an average diameter of ≈60 nm. The hydrodynamic diameter of the PEG encapsulated nanoconstruct was measured by dynamic light scattering (DLS) to be ≈87 nm. Furthermore, photostability of the nanoconstruct under prolonged continuous laser irradiation (in both PA and SERS) for 5 min is shown in Figure S11, Supporting Information. The obtained stable PA and SERS signals indicate the excellent photostability of the nanoconstruct.

2.6. Cell Viability of the Nanoconstruct

Before introducing the nanoconstruct into animals, their cytotoxicity was assessed on oral squamous carcinoma cell line

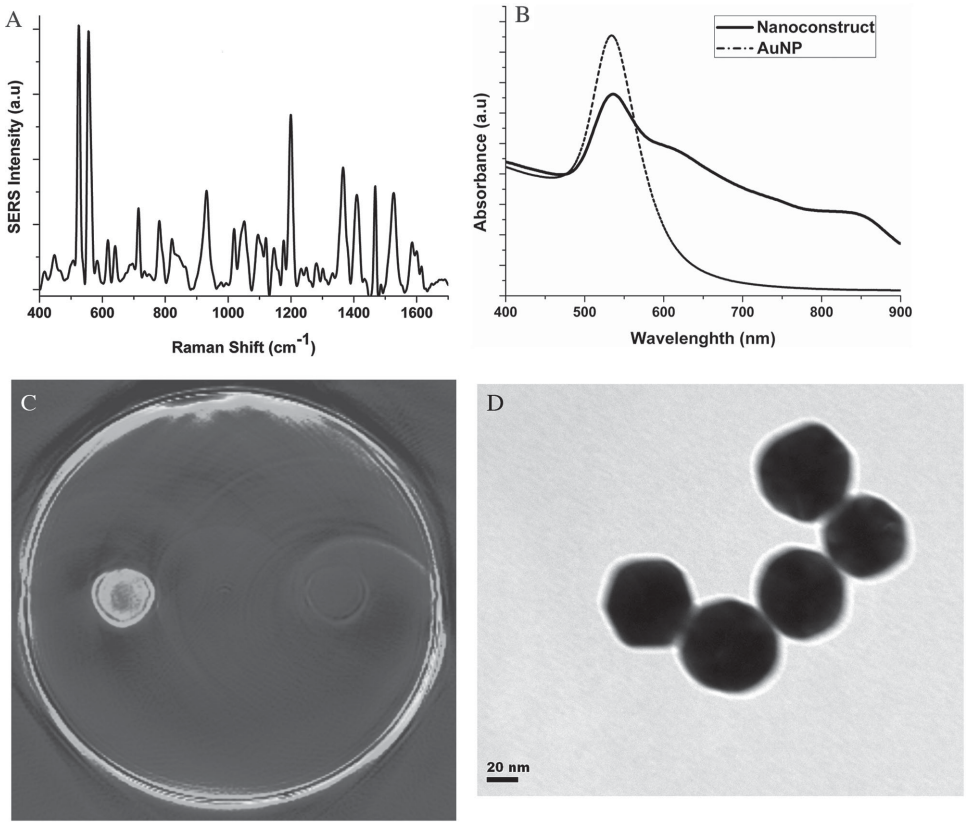

Figure 2. A) SERS spectra of the nanoconstruct with Cy7-lip reporter molecule. B) Absorption spectra of the nanoconstruct. C) PA study of the nanoconstruct in phantom – the bright spot on the left represents the PA signal while the right side circle represents the control. D) TEM image of the PEG encapsulated nanoconstruct.

(OSCC) cells. 100 µL of 1 OD unit of AuNPs, PEG encapsulated nanoconstruct (Probe-PEG), and epidermal growth factor receptor (EGFR) antibody conjugated nanoconstruct (Probe-w ab) were incubated with the cells for 3 h and cell viability was measured after 24 and 48 h. All the particles exhibited close to 100% viability at both time points as shown in **Figure 3**.

2.7. Multimodal In Vivo Tumor Detection

2.7.1. PA Imaging

Nanoconstruct with Cy7-lip as RM was conjugated with anti-EGFR antibody for targeted detection of EGFR biomarker in OSCC xenograft model. This bioconjugated nanoconstruct was injected (200 µL) into the tail vein of the mouse, which served as the test group (targeted) animals while animals injected with nanoconstructs without antibody conjugation served as the control group (nontargeted) animals. After injection of the nanoconstruct, both longitudinal PAI and SERS detection were carried out at the targeted tumor location along with other anatomical organs such as the liver, spleen, and kidney. PA signals were collected at 6 different excitation wavelengths 680, 700, 750, 800, 850, and 900 nm based on the absorption maxima and minima of the nanoconstruct, oxy- and deoxy-hemoglobin at 1, 4, 6, 24, 48, 72, and 96 h post-injection.

Non-background-corrected maximum intensity projection (MIP) PA images of transverse slices through the mouse at two

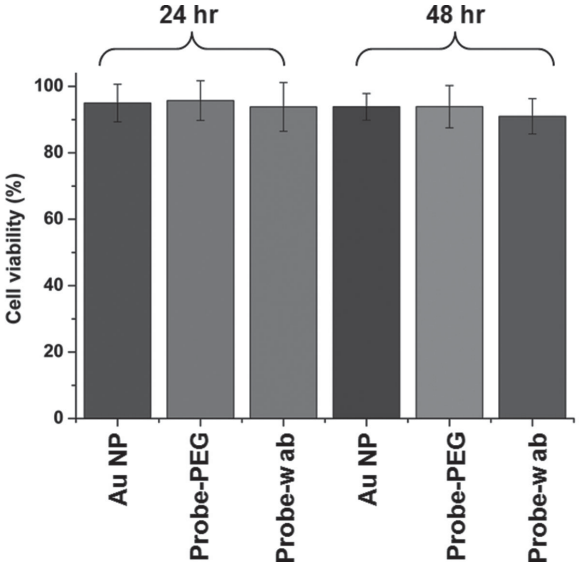

Figure 3. Cell viability study using Cell Counting Kit-8 on OSCC cells exposed to pure AuNPs, PEG encapsulated nanoconstruct (Probe-PEG) and antibody-conjugated nanoconstruct (Probe-w ab) after 24 and 48 h.

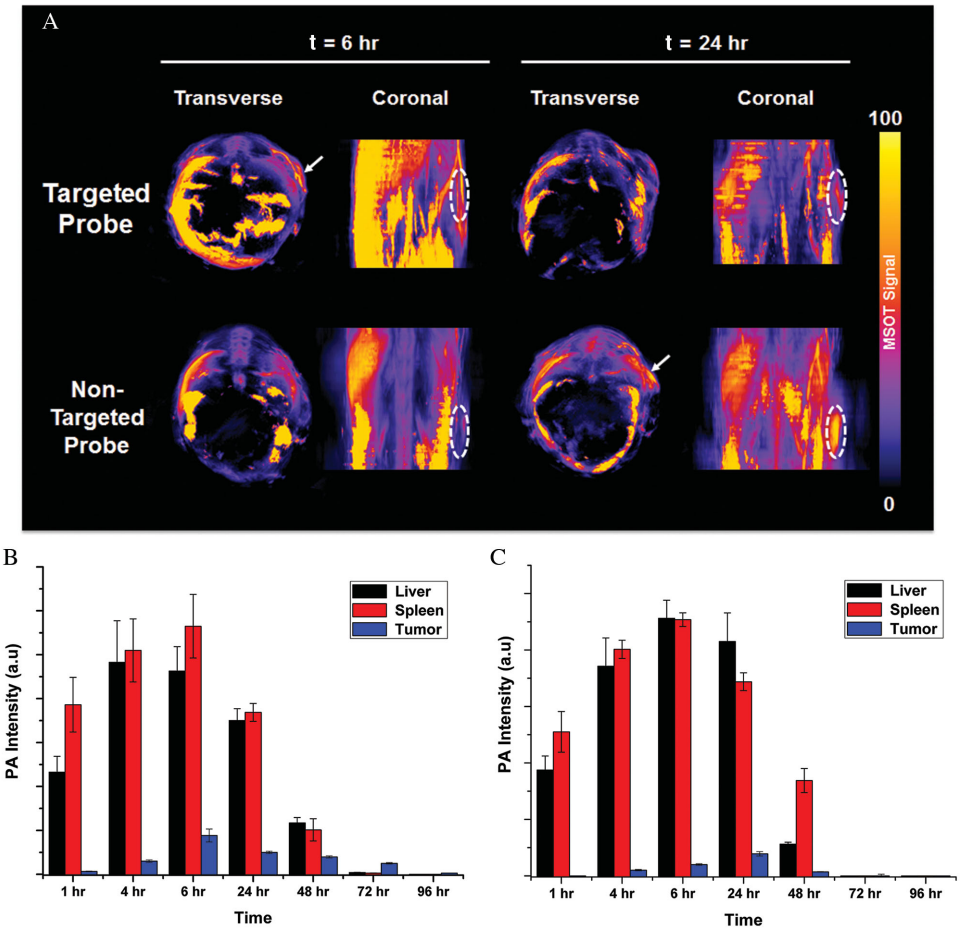

Figure 4. A) In vivo MIP transverse and coronal images of mouse at $t = 6$ and 24 h post injection of the nanoconstruct. The white solid arrows and dotted ellipses show peak probe accumulation at the tumor site for a targeted probe at $t = 6$ h, and a nontargeted probe at $t = 24$ h. The low background MSOT signal (purple) is attributed to intrinsic tissue absorption. Semi-quantitative biodistribution of the probe measured by PA signal intensity at various time points from B) targeted and C) nontargeted probes.

time points (6 and 24 h post-injection) for targeted and nontargeted probe at the tumor site are shown in **Figure 4**A. It can be seen that the nanoconstruct undergoing the active targeting at the tumor location showed maximum signal at 6 h while the nontargeted nanoconstruct showed maximum tumor accumulation at 24 h. This implies faster localization of the conjugated probe, as compared to that of the nontargeted probe at the tumor. This is mainly due to the weak localization of the nontargeted probe in the tumor via enhanced permeation and retention (EPR) effect, where it generally requires 6 to 24 h to reach the maximum.[39,40] Complete MIP transverse images at all the time points for both targeted and nontargeted nanoconstruct are shown in Figures S12 and S13, Supporting Information, while corresponding intensity values at a given region of interest (ROI) in the various organs are plotted in Figure 4B (targeted) and Figure 4C (nontargeted). The accumulation of the targeted probe at the tumor site during the first few hours after injection could be attributed to the active antibody-mediated targeting instead of the EPR effect. Moreover, the PA signal at the tumor site was stronger (≈3 times) for targeted probes. Probe signal at tumor site in test group animals showed gradual reduction after 6 h and negligible signal was observed at 96 h. On the other hand, nontargeted nanoconstruct showed relatively shorter retention of the particles at the tumor site, when compared to targeted probe. Moreover, we also observed that the peak tumor-to-muscle ratio of the PA signal was ≈5 for the targeted probe at the 6 h time point.

Semi-quantitative biodistribution and clearance study of the NPs in the liver and spleen was also successfully studied and evaluated using PAI. PA signal from the probe could be detected in the liver and spleen immediately after the injection in both the test and control group animals. PA signal in the liver and spleen was found to be much stronger than that from the tumor location, which is well in agreement with reported in vivo studies of NPs having size more than 20 nm.[41] Maximum signal was observed at ≈4–6 h and after that it gradually decreased. In both test and control group animals, signal was barely detectable from these passively targeted particles by ≈72 h. We could not measure any considerable signal from the kidney as well, which indicates that the clearance of the particle may be via the reticuloendothelial system (RES). This is primarily due to the size of the particle and in typical cases, in order to have clearance through kidney, the size should be less than 10 nm,[42] while in our case, the conjugated NPs have a size of ≈60 nm.

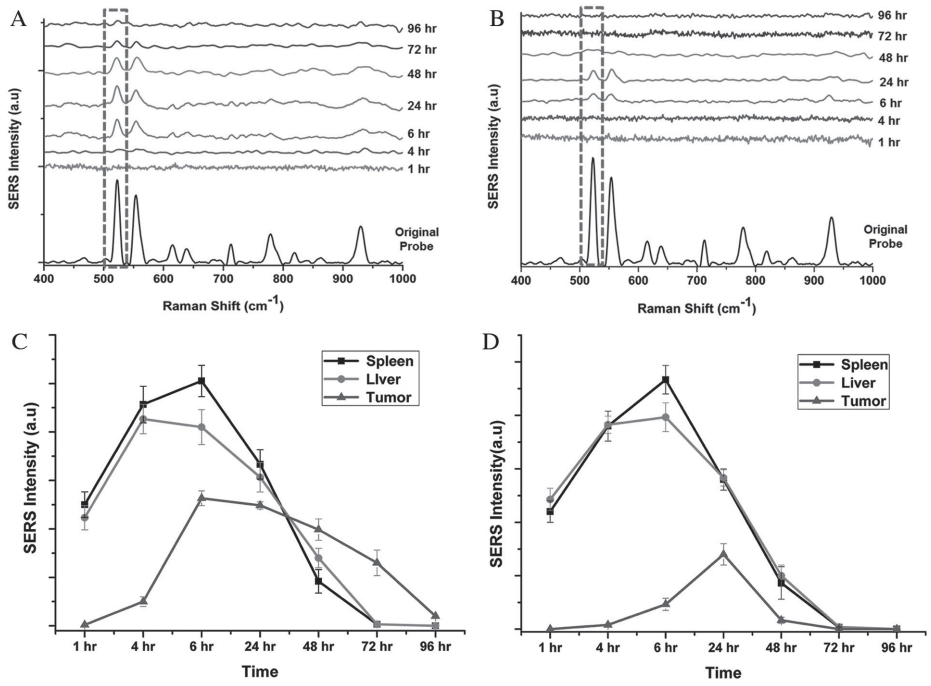

Figure 5. SERS spectra from the tumor site using A) a targeted probe and B) a nontargeted probe at various time points. SERS intensity of 523 cm^{-1} peak of nanoconstruct is marked. Targeted probe show the maximum signal in tumor at 6 h while for the nontargeted probe it is at 24 h followed by gradual decrease. Semi-quantitative biodistribution of the nanoconstruct measured by monitoring the intensity of 523 cm^{-1} peak at various time points using C) targeted and D) nontargeted probes.

2.7.2. SERS Detection

The ultrasensitive sensing capability of SERS is quite useful in the trace detection of biomarkers. In this context, we used SERS to compliment the PAI to understand the probe localization and retention in the targeted location in vivo. As a molecular sensing tool, SERS could provide better sensitivity than any imaging modality such as PA. As shown in **Figure 5**A,B, actively targeted NPs in the tumor showed the highest signal at ≈6 h, while nontargeted NPs in control group animals showed the maximum signal at ≈24 h followed by gradual decrease (SERS spectra are acquired in the 400–1000 cm^{-1} region). Semi-quantitative longitudinal SERS intensity response of both the targeted and nontargeted probes are shown in Figure 5C,D, by measuring the intensity of 523 cm^{-1} peak of the nanoconstruct. In test group animals, probe signal at tumor was ≈2.5 times stronger than that in control animals. Since in vivo SERS detection was achieved through point measurement, there may be a variation in absolute intensity at different depths of the tumor. As we observed in PAI, SERS signals in tumor also showed similar trend with longer retention in the case of targeted probes, when compared to that in the nontargeted probes.

Semi-quantitative biodistribution of the NPs in the liver and spleen followed exactly similar trend as that observed in PAI. SERS measurement revealed that signal from the spleen was slightly higher than that from liver. SERS signal from these organs in test and control groups showed the highest signal intensities at ≈4–6 h and then decreased gradually with no detectable signal by ≈72 h (Figure 5C,D). Our observation in PAI and SERS suggests that these NPs could be taken up by Kupffer cells and might have been excreted through the fecal pathway, which is in agreement with the report on the excretion of the bioconjugated Au-NPs.[43,44] In addition, reticuloendothelial system of the animal can also phagocyte these types of particles, which can later be moved into the liver and excreted as feces with bile.[44]

3. Conclusions

We designed and synthesized a group of NIR active cyanine molecules, which concurrently exhibit both strong Raman and PA activities. Among these three molecules, Cy7-Cl produced the highest PA and SERS signal. Subsequently this molecule was modified with LA moiety and used to construct the nanoprobe to be simultaneously used in both PAI and SERS sensing. This nanoconstruct showed excellent stability in terms of SERS and PA signal up to 3 weeks. Antibody was conjugated to this nanoconstruct for targeted detection of the biomarker in vivo. This bioconjugated nanoconstruct exhibited excellent cell viability. As a proof-of-concept, in vivo noninvasive molecular imaging and sensing of EGFR biomarker was carried out in a mouse xenograft model. Our study showed that targeted probes exhibited the maximum accumulation in tumor by ≈6 h post injection and led to longer retention. On the other hand, nontargeted probes showed the maximum signal in tumor by ≈24 h, which is mainly due to the passive localization via EPR. Moreover, these particles exhibited shorter retention compared to the targeted probe. This trend was validated and confirmed by both SERS sensing and PAI. Semi-quantitative biodistribution of the NPs in liver and spleen showed that these

particles might have been cleared from the mouse body by ≈72 h, possibly via fecal pathway.

In future, we envision that the complimentary imaging and sensing capabilities offered by PA and SERS could help in the identification of the tumor tissues residing under the surface of normal tissues and further to completely remove microscopic tumor deposits. This dual imaging modality could offer both diagnostic and prognostic imaging options along with image-guided resection.

4. Experimental Section

Materials: All chemicals and reagents were commercially available and used as received without further purification. Anhydrous *N,N*-dimethylformamide (DMF) and acetonitrile (ACN) were purified by Innovative Solvent Purification System. Toluene and dichloromethane (DCM) were distilled from sodium benzophenone ketyl and calcium hydride, respectively, under nitrogen immediately prior to use. *n*-Butanol (*n*-BuOH) was dried by anhydrous magnesium sulfate before use. Dicyclohexylcarbodiimide (DCC), lipoic acid (LA), and iodoethanol were purchased from Aldrich. Phosphorus oxychloride ($POCl_3$) and *p*-toluene sulfonic acid (TsOH) monohydrate were purchased from International Laboratory and Meryer, respectively. Commercially available MGITC (Life technologies) and Rh6G (sigma) were purchased. Cy5 was synthesized in the lab.[45]

Absorbance Measurement: UV–vis absorption spectra were obtained with Hitachi U-2900 spectrometer with a double-beam optical system and spectral band pass of 1.5 nm and the measured spectrum was used as an input spectrum to be used for multispectral post-processing of PA signals.

TEM and DLS Measurement: TEM images were taken using the JEOL JEM-1010 machine. Acceleration voltage was 40–100 kV and stability was 2 ppm min^{-1}. The magnification range of the instrument covers from 50 to 600 000× with a resolution of 0.3000 nm. Images of the PEG encapsulated nanoconstructs were taken at a 250 000× magnification. DLS measurement was carried out using Zetasizer (Malvern instruments, Nano-ZS).

Preparation of Nanoconstruct and Bioconjunction: The nanoconstruct was realized with Cy7-lip as RM. Cy7-lip (dissolved in DMSO) solutions at various concentrations (100×10^{-6}, 50×10^{-6}, 30×10^{-6}, 20×10^{-6}, 10×10^{-6}, 5×10^{-6}, and 1×10^{-6} M) were mixed with 60 nm AuNPs (BB International, 2.6×10^{10} particles mL^{-1}) in 1:9 v/v ratio for 15 min. Optimization of the concentration of RM was carried out to yield stable and high SERS signal with minimal colloidal aggregation. LA linker on the RM can chemisorb on to AuNPs by thiol linkage and results in stable SERS signal.[45] Excess and unbound RMs were removed by centrifugation. The number of RMs attached onto AuNPs was estimated to be ≈13000, which is in accordance with previous similar reports.[29,30] We then employed PEG encapsulation for antibody conjugation and also for the protection of the nanoconstruct. Thiolated-carboxylated PEG (HS-PEG-CO_2H, 10×10^{-6} M, RAPP Polymere GmbH) was first added drop by drop to the AuNP-RM conjugate and mixed for 20 min. Subsequently, thiolated PEG (PEG-SH, 10×10^{-6} M, RAPP Polymere GmbH) was added slowly to the mixture and incubated for 3 h. Later, the solution was centrifuged to remove the excess PEG and re-suspended in PBS. To achieve antibody bioconjugation on the particles, carboxylic acid functional group on the surface of these PEG encapsulated particles was activated by ethyl dimethylaminopropyl carbodiimide (EDC) and sulfo-N-hydroxysuccinimide (NHS) coupling reaction. To achieve this, 10 µL of EDC (25×10^{-3} M in water) and NHS (25×10^{-3} M in water) were added to the PEG encapsulated NP solution and mixed for 20 min. The excess amount of EDC and NHS was removed by centrifugation and then the solution was re-suspended in PBS. Finally, anti-EGFR antibody (100 µL, 200 µg mL^{-1}, Santa Cruz, sc-120) was reacted with activated with Cy7-lip nanoconstruct at 25 °C for 2 h and then kept for overnight incubation at 4 °C. Finally, nonspecifically bound antibodies were removed and the bioconjugated nanoconstruct was stored at 4 °C. On average, there are ≈500 antibodies anchored to each AuNP.

Cell Culture and Cell Viability: Human metastatic oral squamous carcinoma cell line (OSCC) was maintained in DMEM supplemented with 10% fetal bovine serum (FBS) and 1% antibiotic – antimycotic solution. Cells were used for cytotoxicity assay at 80% confluence. For cell viability study, 1×10^4 cells were seeded per well in a 96 well plate. 100 µL of 1 OD unit of AuNPs and PEG encapsulated nanoconstruct formulations with and without antibody conjugation were added in at least triplicates and incubated for 3 h. After discarding the free nanotags, cells were replenished with complete DMEM, incubated for 24 and 48 h and measured for cell viability using Cell Counting Kit – 8 (CCK-8, Sigma). In this study, cells incubated with AuNPs were used as control.

Mouse Xenograft: Balb/c nude female mice (4–6 weeks old) obtained from the Biological Resource Centre (Biomedical Sciences Institute, A*STAR) were inoculated subcutaneously on the right flank with 5×10^6 OSCC cells mixed in 1:1 ratio with Matrigel (BD Biosciences) in a volume of 100 µL. After 2 weeks, when the tumors grew to a palpable size, 200 µL of the antibody conjugated (test group, targeted) and nonantibody conjugated (control group, nontargeted) nanoconstruct were injected into the tail vein of the mouse. PAI and SERS experiments were conducted in total of 4 animals. All animal experimental procedures were performed in accordance with protocol #120774 approved by the Institutional Animal Care and Use Committee (IACUC).

PA Imaging (Instrumentation): All PA imaging experiments were performed using a commercial 128-channel real-time multispectral optoacoustic tomographic (MSOT) imaging system (iThera Medical GmbH). Optical excitation was provided by an optical parametric oscillator with a tunable NIR wavelength range from 680 to 980 nm, which was in turn pumped by a Q-switched Nd: YAG laser with a pulse duration of 10 ns and repetition rate of 10 Hz. Light was delivered by a fiber bundle divided into 10 output arms to illuminate the sample from multiple angles around the imaging plane. PA signals were acquired using a 128-element concave transducer array spanning a circular arc of 270°. This transducer array has a central frequency of 5 MHz, which gives a transverse spatial resolution of ≈150–200 µm. One transverse image slice was acquired from each laser pulse, resulting in a frame-rate of 10 Hz. During image acquisition, the sample was translated through the transducer array along its axis across the volume ROI, in order to capture the corresponding transverse image slices. All the image reconstruction and post processing of data was carried out using the associated View MSOT software version 3.2.

Phantom Measurement: In order to evaluate the PA activity of the cyanine molecules, we performed the study in a phantom (iThera Medical). This phantom is cylindrical in shape and made of polyurethrane material, with tissue-mimicking optical properties. It has a diameter of 2 cm and contains 2 channels in which test molecules and control can be placed. Initially, all the three molecules (Cy7-Cl, Cy7 (S)-Cl, and Cy7-OTPE, all dissolved in DMSO) were tested at a concentration of 5×10^{-6} M and DMSO was used as the control. Data from multiple transverse slices across the channel that contains the test molecule and control were measured within an excitation wavelength scanning range from 680 to 900 nm, with an interval of 10 nm for each transverse slice. Averaged PA signals from 10 frames for each wavelength and position were detected. Similarly, nanoconstruct with Cy7-lip as the reporter molecule was also tested in the phantom by using AuNPs as the control. Image reconstruction was carried out to evaluate the PA activity of the molecule with respect to the control solution.

In Vivo Longitudinal Imaging: Tumor-bearing mice was anaesthetized under isoflurane and injected with the nanoconstruct via the tail vein. Subsequently, ultrasound gel was applied on the mouse skin surface and in vivo imaging was carried out in a temperature-controlled water medium for optimal acoustic coupling. An animal holder with a thin polyethylene membrane was used to prevent direct contact between the mouse and the water. Animal was kept under isoflurane and localization and biodistribution of the nanoconstruct were studied over time in various organs. Before image acquisition, a volume ROI consisting of transverse slices through various organs with a step size of 0.3 mm spanning from

the liver to the lower abdomen was selected by manual inspection of live MSOT images. Six laser wavelengths of 680, 700, 750, 800, 850, and 900 nm were selected for excitation, based on the absorption spectra of the nanoconstruct and endogenous absorbers such as oxy- and deoxy-haemoglobin. Multispectral imaging was then performed with 10 signal averages per wavelength per transverse slice at various time points (before injection, 1, 4, 6, 24, 48, 72, and 96 h after injection).

Image Reconstruction and Multispectral Processing: Images were reconstructed using a model-based approach for offline analysis. After image reconstruction, spectral unmixing was performed to resolve individual components from different absorbers in the system. For each pixel in the image, the method fits the total measured optoacoustic spectrum to the known absorption spectra of the individual absorbers, based on least-squares linear regression.

Image Processing: Maximum intensity projection (MIP) images at t = 6 and 24 h were prepared in both transverse and coronal planes for better display of anatomy and quantification. A MIP is a volume rendering method for 3D data that projects in the visualization plane of the voxels with maximum intensity that fall in the way of parallel rays traced from the viewpoint to the plane of projection. Although a MIP is a 2D projection of 3D data which results in some information loss, image correlation and validation between MIPs from both transverse and coronal planes overcomes this issue and helps to identify regions of probe localization in various organs and the tumor site.

SERS Measurements (Instrumentation): SERS spectral measurements were carried out using a Raman microscope (Renishaw InVia, UK) at an excitation wavelength of 785 nm. The laser is coupled to a Leica microscope and the beam is directed to the sample through a 50× or 20× objective lens and a Peltier cooled CCD detector was used to collect the SERS signals. The WiRE 3.2 software package provided with the system was employed for instrument control and data acquisition. Stokes shifted Raman spectra were collected in the range of 400–1700 cm^{-1} with a resolution of about 1 cm^{-1} and the exposure time was set at 10 s for all in vitro measurements. The shutter of the laser was immediately closed after each measurement to minimize any possible photodamage of the sample under a prolonged illumination. Baseline correction of the measured spectra was performed to remove the broad background and fluorescence band. Prior to each measurement, the instrument was calibrated with a silicon standard whose Raman peak is centered at 520 cm^{-1}.

Spectral Measurements: Initially SERS spectra of the three RMs (Cy7-Cl, Cy7 (S)-Cl, and Cy7-OTPE) were measured after mixing 10×10^{-6} M solution (in DMSO) with 60 nm AuNPs (BB International, 2.6×10^{10} particles mL^{-1}) in 1:9 v/v ratio and incubating for 15 min. 20 µL of the reporter-Au NP mixture solutions were placed on a clean glass slide with a cover slip and measured under the Raman microscope at 785 nm excitation (50 µW and 10 s integration time). Spectral measurements were repeated three times from one single sample preparation. SERS spectral measurements of nanoconstruct with Cy7-lip nanoconstruct were also carried out at 785 nm excitation (50 µW and 10 s integration time).

In Vivo SERS Detection: Immediately after PAI measurement, tumor bearing mouse (injected with antibody conjugated and nonantibody conjugated nanoconstruct) was anesthetized by intraperitoneal injection of ketamine (150 mg kg^{-1})/xylazine (10 mg kg^{-1}) and kept under Raman microscope for in vivo detection at various time points. In vivo SERS spectra were acquired five times on tumor site, liver, and spleen using 30 mW, 785 nm laser excitation through a 20× objective lens. The same lens was used to collect the Stokes shifted Raman signal. Experiments were conducted in total on 4 animals under test and control groups. All animal experimental procedures were performed in accordance with protocol #120774 approved by the Institutional Animal Care and Use Committee (IACUC).

Supporting Information

Supporting Information is available from the Wiley Online Library or from the author.

Acknowledgements

U.S.D. and Z.S. contributed equally to this work. We thank the Singapore Bioimaging Consortium (SBIC), A*STAR, Singapore Ministry of Education (R279–000–391–112), Singapore NRF Investigatorship, the Research Grants Council of Hong Kong (HKUST2/CRF/10), the Ministry of Science and Technology of China (973 program 2013CB834701), and Guangdong Innovative Research Team Program (201101C0105067115) for financial support. The authors also would like to thank Mr. Yu Yang and Miss Ruchi (Industrial attachment students from Nanyang Technological University, Singapore) for their help in this project.

Received: December 8, 2014
Revised: February 4, 2015
Published online: March 11, 2015

[1] R. Weissleder, *Science* **2006**, *312*, 1168.
[2] S. S. Gambhir, *Nat. Rev. Cancer.* **2002**, *2*, 683.
[3] S. Keren, C. Zavaleta, Z. Cheng, A. de la Zerda, O. Gheysens, S. S. Gambhir, *Proc. Natl. Acad. Sci. U.S.A.* **2008**, *105*, 5844.
[4] S. Lee, S. Kim, J. Choo, S. Y. Shin, Y. H. Lee, H. Y. Choi, S. Ha, K. Kang, C. H. Oh, *Anal. Chem.* **2007**, *79*, 916.
[5] K. Faulds, R. P. Barbagallo, J. T. Keer, W. E. Smith, D. Graham, *Analyst* **2004**, *129*, 567.
[6] M. H. J. G. W. Sark van, M. T. L. P. Frederix, J. D. Heuvel Vanden, C. H. Gerriten, *J. Phys. Chem. B* **2001**, *105*, 8281.
[7] M. Xua, L. V. Wang, *Rev. Sci. Instrum.* **2006**, *77*, 041101.
[8] M. A. Pysz, S. S. Gambhir, J. K. Willmann, *Clin. Radiol.* **2010**, *65*, 500.
[9] L. V. Wang, *Nat. Photonics* **2009**, *3*, 503.
[10] C. Kim, C. Favazza, L. V. Wang, *Chem. Rev.* **2010**, *110*, 2756.
[11] J. Levi, S. R. Kothapalli, T. J. Ma, K. Hartman, B. T. Khuri-Yakub, S. S. Gambhir, *J. Am. Chem. Soc.* **2010**, *132*, 11264.
[12] A. Abuteen, S. Zanganeh, J. Akhigbe, L. P. Samankumara, A. Aguirre, N. Biswal, M. Braune, A. Vollertsen, B. Roder, C. Bruckner, Q. Zhu, *Phys. Chem. Chem. Phys.* **2013**, *15,* 18502.
[13] D. Razansky, A. Buehler, V. Ntziachristos, *Nat. Protocols.* **2011**, *6*, 1121.
[14] A. De la Zerda, C Zavaleta, S. Keren, S. Vaithilingam, S. Bodapati, Z. Liu, J. Levi, B. R. Smith, T. J. Ma, O. Oralkan, Z. Cheng, X. Chen, H. Dai, B. T. Khuri-Yakub, S. S. Gambhir, *Nat. Nanotechnol.* **2008**, *3*, 557.
[15] A. De la Zerda, Z. Liu, S. Bodapati, R. Teed, S. Vaithilingam, B. T. Khuri-Yakub, X. Chen, H. Dai, S. S. Gambhir, *Nano Lett.* **2010**, *10*, 2168.
[16] E. Herzog, A. Taruttis, N. Beziere, A. A. Lutich, D. Razansky, V. Ntziachristos, *Radiology* **2012**, *263*, 461.
[17] A. Taruttis, S. Morscher, N. C. Burton, D. Razansky, V. Ntziachristos, *PLoS One* **2012**, *7*, e30491.
[18] L. Nie, S. Wang, X. Wang, P. Rong, Y. Ma, G. Liu, P. Huang, G. Lu, X. Chen, *Small* **2014**, *10*, 1585.
[19] A. Taruttis, E. Herzog, D. Razansky, V. Ntziachristos, *Opt. Express* **2010**, *18*, 19592.
[20] J. V. Jokerst, A. J. Cole, D. Van de Sompel, S. S. Gambhir, *ACS Nano* **2012**, *11*, 10366.
[21] K. W. Kho, C. Y. Fu, U. S. Dinish, M. Olivo, *J. Biophotonics* **2011**, *4*, 667.
[22] Y. Zhang, H. Hong, D. V. Myklejord, W. Cai, *Small* **2011**, *7*, 3261.
[23] W. Xie, S. Schlucker, *Phys. Chem. Chem. Phys.* **2013**, *15*, 5329.
[24] K. C. Bantz, A. F. Meyer, N. J. Wittenberg, H. Im, O. Kurtulus, S. H. Lee, N. C. Lindquist, S. H. Oh, C. L. Haynes, *Phys. Chem. Chem. Phys.* **2011**, *13*, 11551.
[25] C. L. Zavaleta, B. R. Smith, I. Walton, W. Doering, G. Davis, B. Shojaei, M. J. Natan, S. S. Gambhir, *Proc. Natl. Acad. Sci. U.S.A.* **2009**, *106*, 13511.

[26] K. K. Maiti, U. S. Dinish, A. Samanta, M. Vendrell, K. S. Soh, S. J. Park, M. Olivo, Y. T. Chang, *Nano Today* **2012**, *7*, 85.
[27] J. A. Dougan, K. Faulds, *Analyst* **2012**, *137*, 545.
[28] U. S. Dinish, G. Balasundaram, Y. T. Chang, M. Olivo, *J. Biophoton.* **2014**, *7*, 956.
[29] X. Qian, X. H. Peng, D. O. Ansari, Q. Y. Goen, G. Z. Chen, D. M. Shin, L. Yang, A. N. Young, M. D. Wang, S. Nie, *Nat. Biotechnol.* **2008**, *26*, 83.
[30] K. K. Maiti, U. S. Dinish, C. Y. Fu, J. J. Lee, K. S. Soh, S. W. Yun, R. Bhuvaneswari, M. Olivo, Y. T. Chang, *Biosens. Bioelectron.* **2010**, *26*, 398.
[31] A. Samanta, K. K. Maiti, K. S. Soh, X. Liao, M. Vendrell, U. S. Dinish, S. W. YunR. Bhuvaneswari, H. Kim, S. Rautela, J. Chung, M. Olivo, Y. T. Chang, *Angew. Chem. Int. Ed.* **2011**, *50*, 6089.
[32] B. Kustner, M. Gellner, M. Schutz, F. Schoppler, A. Marx, P. Strobel, P. Adam, C. Schmuck, S. Schlucker, *Angew. Chem. Int. Ed.* **2009**, *48*, 1950.
[33] U. S. Dinish, G. Balasundaram, Y. T. Chang, M. Olivo, *Sci. Rep.* **2014**, *4*, 4075.
[34] M. F. Kircher, A. de la Zerda, J. V. Jokerst, C. L. Zavaleta, P. J. Kempen, E. Mittra, K. Pitter, R. Huang, C. Campos, F. Habte, R. Sinclair, C. W. Brennan, I. K. Mellinghoff, E. C. Holland, S. S. Gambhir, *Nat. Med.* **2012**, *18*, 829.
[35] K. Yang, H. Xu, L. Cheng, C. Sun, J. Wang, Z. Liu, *Adv. Mater.* **2012**, *24*, 5586.
[36] Y. Wang, B. Yan, L. Chen, *Chem. Rev.* **2013**, *113*, 1391.
[37] S. S. Ramos, P. F. Santos, L. V. Reis, P. Almeida, *Dyes Pigments* **2002**, *53*, 143.
[38] R. Wang, F. Yu, L. Chen, H. Chen, L. Wang, W. Zhang, *Chem. Commun.* **2012**, *48*, 11757.
[39] H. Maeda. *Adv. Enzym. Regul.* **2001**, *41*, 189.
[40] H. Maeda, H. Nakamura, J. Fang, *Adv. Drug. Delivery Rev.* **2013**, *65*, 71.
[41] J. P. M. Almeida, A. L. Chen, A. Foster, R. Drezek, *Nanomedicine* **2011**, *6*, 815.
[42] M. Longmire, P. L. Choyke, H. Kobayashi, *Nanomedicine* **2008**, *3*, 703.
[43] G. Renand, R. L. Hamilton, J. R. Havel, *Hepatology* **1989**, *9*, 380.
[44] K. T. Yong, I. Roy, H. Ding, E. J. Bergey, P. N. Prasad, *Small* **2009**, *5*, 1997.
[45] K. K. Maiti, A. Samanta, M. Vendrell, K. S. Soh, M. Olivo, Y. T. Chang, *Chem. Commun.* **2011**, *47*, 3514.